Journal of Sedimentary Research

Journal of Sedimentary Research, 2021, v. 91, 390–398
Research Methods
DOI: 10.2110/jsr.2020.114

A NOVEL APPROACH TO INVESTIGATE THE DEPOSITION OF (BIO)CHEMICAL SEDIMENTS: THE SEDIMENTATION VELOCITY OF CYANOBACTERIA–FERRIHYDRITE AGGREGATES

YUHAO LI,[1] BRUCE R. SUTHERLAND,[2,1] MURRAY K. GINGRAS,[1] GEORGE W. OWTTRIM,[3] AND KURT O. KONHAUSER[1]
[1] Department of Earth and Atmospheric Sciences, University of Alberta, Edmonton, Alberta T6G 2E3, Canada
[2] Department of Physics, University of Alberta, Edmonton, Alberta T6G 2E1, Canada
[3] Department of Biological Sciences, University of Alberta, Edmonton, Alberta T6G 2E3, Canada

ABSTRACT: **Sedimentation velocities of various chemical sediments are typically calculated using Stokes's law. However, applying it to chemical sediments that form *in situ* in the water column is not ideal because the particle properties do not fulfill many of the assumptions underpinning the applicability of Stokes' law. As a consequence, it has been difficult to predict the sedimentation rate of ancient chemical sediments, such as Precambrian banded iron formations (BIF), because their primary sediments likely comprised aggregates of ferric hydroxides, such as ferrihydrite [$Fe(OH)_3$], and marine bacterial biomass, including cyanobacteria. In this work we use a new experimental method to address the mechanisms by which primary BIF sediment, formed by the oxidation of dissolved Fe(II) by O_2 and simultaneously incubated with cyanobacterium *Synechococcus* sp., were deposited to the Archean ocean. Specifically, we formed the aggregates *in situ* over a wide range of initial pH and Fe(II) concentrations, continuously recorded the entire settling processes of aggregates under each condition, and then processed the data in MATLAB according to different settling mechanisms. Our results demonstrate that ferrihydrite–cyanobacteria aggregates settled to the ocean floor either through the formation of uniformly descending concentration fronts or through convective plumes. The sedimentation mechanism depended on both initial Fe(II) concentration and the pH. Correspondingly, two algorithms were developed to characterize the sedimentation velocity. These algorithms tracked the alteration of light intensity from low to high as sediments descended from an initially homogeneous state through a water tank, and as well calculated the average light intensity over time, from which vertical time series were constructed allowing calculation of the sedimentation velocity. Our method not only provides an accurate estimation of the *in situ* sedimentation velocity of cell–mineral aggregates, but also provides new insights into the physical mechanisms by which the primary sediments composing BIF were deposited.**

INTRODUCTION

Sedimentation velocity refers to the speed at which particles fall through a viscous fluid. Understanding grain-fall behavior is a key factor to understand how sediments settle through the water column in different environments, e.g., rivers, lakes, deltas, estuaries, and pelagic marine settings have a range of abiotic parameters. Studies used to determine the sedimentation velocity of (bio)chemical sediments have typically measured the average size and density of sediments and subsequently applied Stokes' Law, which defines the terminal velocity of a spherical particle descending through a uniform balance of buoyancy and viscous forces (Konhauser et al. 2005; Posth et al. 2010; Thompson et al. 2019). The steady velocity is a function of gravity, particle density, fluid density, fluid viscosity, and particle radius (Stokes 1850; Arnold 1911). For a sufficiently small and slowly descending spherical particle, the viscous force exerted has a defined magnitude, given by $F\mu = 6\pi\mu r Us$, where μ is the molecular viscosity of the fluid, r is the radius of the spherical particle, and Us is the sedimentation velocity. Also acting on the particle is the buoyancy force, $F_b = \frac{4}{3}\pi r^3(\rho_P - \rho_f)g$, which is the difference between the weight of the particle and of the fluid it displaced. Here, ρ_P is the particle density, ρ_f is the fluid density, and g is the acceleration of gravity. The terminal velocity predicted by Stokes' law results when the viscous force is equal and opposite to the (negative) buoyancy force, and is given by

$$Us = \frac{2}{9} \times \frac{(\rho_P - \rho_f) \cdot g \cdot r^2}{\mu} \quad (1)$$

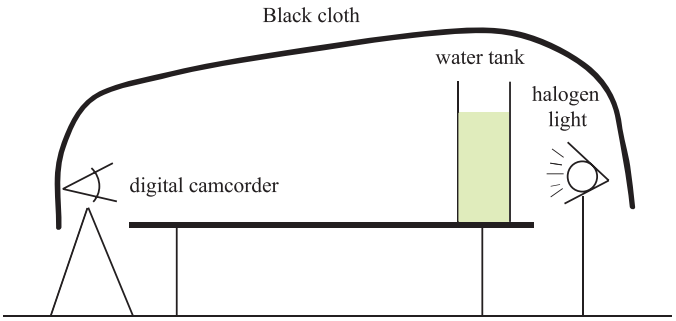

FIG. 1.—Setup of settling experiment.

Published Online: April 2021
 1527-1404/21/091-390

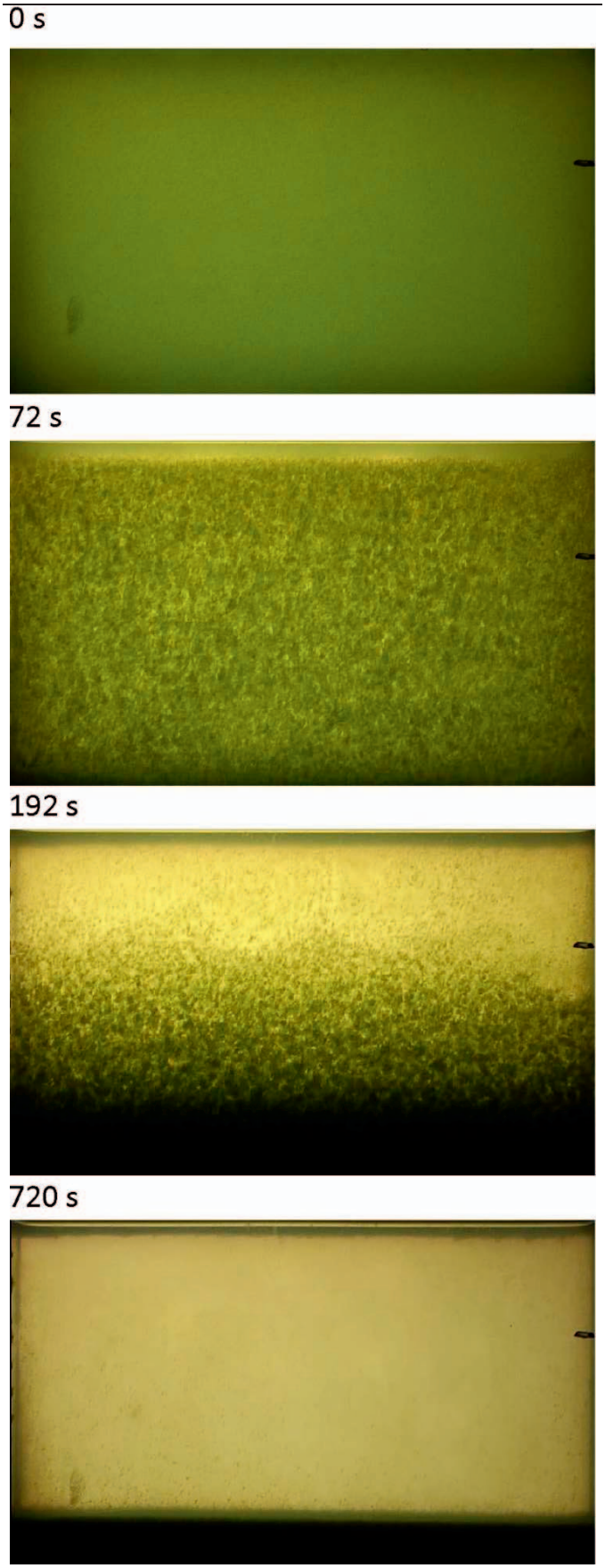

There are several assumptions leading to the derivation of the terminal velocity, including the following: 1) the Reynolds number, $\mathrm{Re} = \rho_f U s r / \mu$, is less than 0.1, which means Stokes' law applies only to laminar flows surrounding sufficiently small and slowly settling particles, 2) the particles are rigid spheres, and 3) any surrounding particles are sufficiently separated (typically farther than 10 particle diameters) from the surrounding convective fluid motion that they have negligible influence on the settling of the particle in question (Arnold 1911; Wray 1977). Obviously, these rigid parameters severely limit accurate analysis of sedimentation velocity in natural habitats. In particular, particles that grow out of a solution are not necessarily spherical and can flocculate to form larger aggregates with potentially larger settling velocity. However, if the particle concentration by volume exceeds approximately 1%, then interacting settling particles can hinder their collective settling and lead to unstable, irregular downward and upward flows (Guazzelli and Hinch 2011). In part, here we examine how these complicating and competing factors affect sedimentation of growing aggregates.

In the work presented here, we use the example of ferrihydrite–cyanobacteria aggregates to demonstrate whether an established method that measures the sedimentation velocity of clays is also applicable to (bio)chemical sediments (Sutherland et al. 2015; Playter et al. 2017). We chose these components because they could have provided major contributions to the deposition of banded iron formations (BIF), the iron-rich (15–40 wt.% Fe) and siliceous (40–60 wt.% SiO_2) chemical deposits that formed on the continental shelves throughout the Precambrian Eon (Konhauser et al. 2017). The best-preserved successions are commonly composed of fine-grained quartz (SiO_2), magnetite (Fe_3O_4), and hematite (Fe_2O_3), with variable amounts of Fe-rich silicate and carbonate minerals (Klein 2005; Beukes and Gutzmer 2008; Bekker et al. 2010; Smith et al. 2013, 2017; Konhauser et al. 2017). It is agreed that none of the minerals in BIF are primary in origin in the sense that the original precipitate was likely a hydrous and amorphous precipitate that was transformed postdepositionally during diagenesis and metamorphism. Instead, iron oxides in BIF are generally interpreted to have formed from an initial ferrihydrite phase which precipitated in the photic zone via bacterial oxidation of dissolved ferrous iron; the bacterial role was either direct through anoxygenic photosynthesis or indirect through reaction with cyanobacteria-generated oxygen (Posth et al. 2013, 2015; Smith 2015; Konhauser et al. 2018). However, it should be noted that others have proposed that the primary precipitates to BIF were instead ferrous silicates, such as greenalite (e.g., Rasmussen et al. 2017). If that is true, the precipitation of those minerals would not necessitate a biological role because no Fe(II) oxidation is involved.

Although there is compelling evidence that support the composition comprising BIF primary sediment and that the driving mechanism for Fe(II) oxidation was biological (Robbins et al. 2019), what remains unanswered is: 1) the physical processes by which ferrihydrite–microbes were sedimented, and 2) the rate of particle flocculation through a marine water column likely < 150 meters in depth. Previous studies examining the association between Fe(III) minerals and different anoxygenic, photosynthetic, Fe(II)-oxidizing bacteria, the so-called photoferrotrophs, have consistently shown that the attachment between the Fe minerals and cells is minimal (e.g., Konhauser et al. 2005; Gauger et al. 2016). This is logical because a tight association would lead to a reduction in cell survival resulting from sedimentation out of the photic zone. In the case of the photoferrotrophic bacterium, *Chlorobium phaeoferrooxidans* strain KB01, a photoferrotrophic

←

FIG. 2.—Images from a settling-front experiment with pH = 11 and initial Fe(II) concentration of 1800 μM. In each image the field of view is 20 cm wide by 10 cm tall. Note the color difference between the snapshots at 0 s and 720 s, showing the co-deposition of cyanobacteria cells and ferrihydrite.

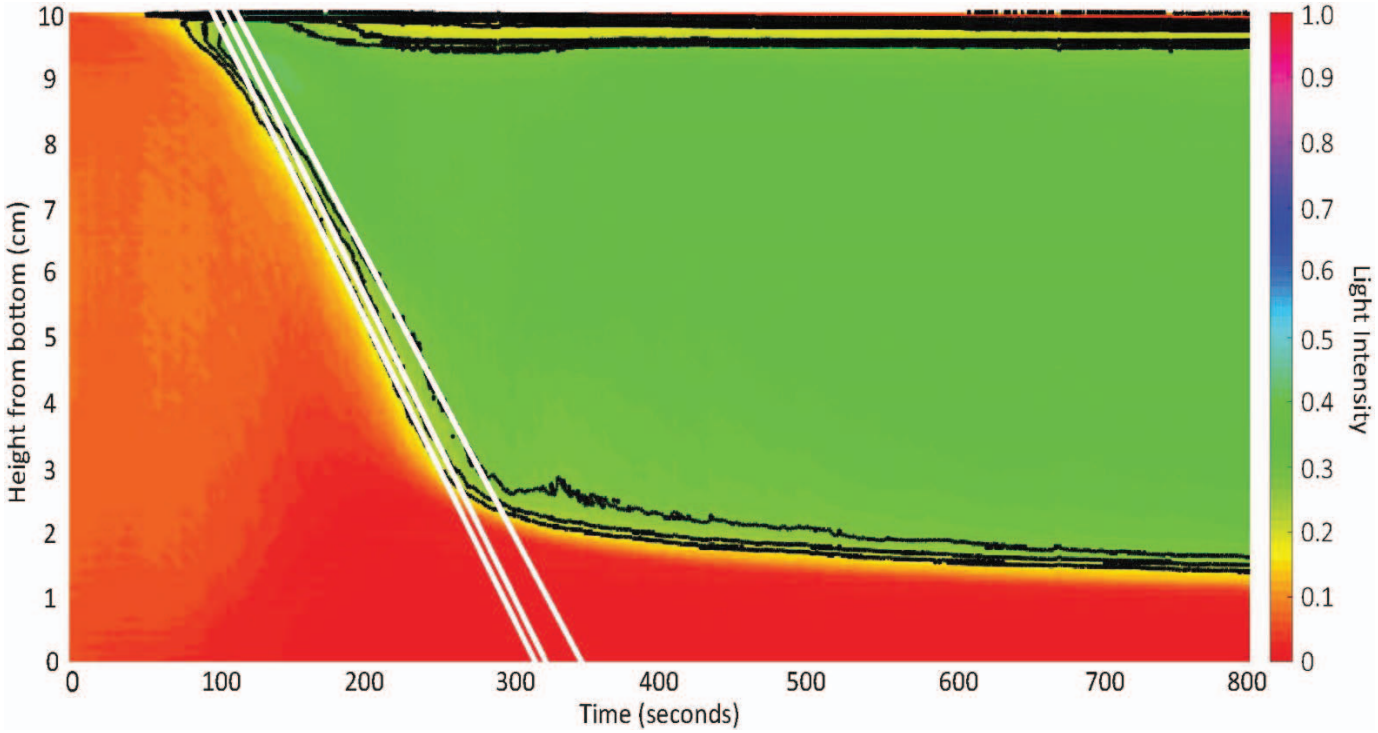

FIG. 3.—Vertical time series of horizontally averaged light intensity taken from the experiment shown in Figure 2.

bacterium that was isolated from the water column of ferruginous Kabuno Bay, a sub-basin of Lake Kivu in East Africa, experiments demonstrated that only 6% of the cells were sedimented in Fe- and Si-rich media used as a modern analogue of Archean seawater composition (Thompson et al. 2019).

Based on a number of photoferrotroph iron-oxidation experiments, particle sizes were generally between 10 to 40 μm (Konhauser et al. 2005; Posth et al. 2010; Schad et al. 2019), with sedimentation velocity using Stokes' Law estimated between from 0.01 cm s^{-1} to 0.24 cm s^{-1}. As predicted, the sedimentation velocity increased with particle size and the Fe:C ratio (which influences particle density); the cell component of the biogenic minerals lowers the total particle density, resulting in a decreased sedimentation velocity (Posth et al. 2010). Interestingly, despite the experiments using a wide range of Fe(II) starting concentrations (from 200 to 1000 μM), a strong trend between initial Fe(II) concentration and aggregate size was not observed.

By comparison to the photoferrotrophs, the only study to date that we are aware of, looking at the interaction of cyanobacteria (specifically *Synechococcus* sp. PCC 7002) with ferrihydrite products of Fe(II) oxidation, demonstrated a strong cell–mineral association (Thompson et al. 2019). This is unsurprising because the O_2 released as a by-product of oxygenic photosynthesis reacts rapidly with Fe(II) at circumneutral pH, causing direct precipitation of ferrihydrite on the cell surface. Moreover, this association was likely facilitated by ferrihydrite binding to organic ligands on the cell's surface (Phoenix et al. 2000). If cyanobacteria, such as *Synechococcus*, were readily encrusted in ferrihydrite, do the mineral–cell aggregates increase sedimentation velocities, and can those velocities be quantified in a more meaningful manner than Stokes' Law? Ultimately, this information is essential for describing the sedimentation velocity of BIF, particularly during the late Archean, when ocean surface waters are believed to have become oxygenated, possibly even below the photic zone (e.g., Kendall et al. 2010).

METHODS

Experimental Design

The experiment design was followed as per Sutherland et al. (2015) and Playter et al. (2017). The experiments were performed in a 30-cm-tall clear acrylic tank with horizontal dimensions of 20 cm × 5.1 cm (Fig. 1). Black construction paper was placed at the back of the water tank from 10 cm above the bottom to the top of the tank. Translucent Mylar sheets were affixed to the back of the tank over the bottom 10 cm, while a halogen light was placed behind the water tank to enhance visualization of the particles during the settling process. A Panasonic HDC-HS250 digital camcorder or a Huawei P30 pro mobile phone were used for recording videos that were shorter than or longer than 1.5 hours, respectively. Continuous movies were recorded at 24 frames per second of the backlit part of the tank. Variations in ambient light were blocked by a black cloth that covered the entire set-up between the camera and tank.

Preparation of Sedimentation Media

Three sedimentation components, consisting of a Si-rich ferrihydrite and cyanobacteria corresponding to the predicted initial composition of BIF sediment, were prepared separately and mixed *in situ* in the water tank. The Fe(II) stock solution (0.2 M) was produced anaerobically from ferrous chloride tetrahydrate. The silica (Si) stock solution (0.2 M) was made from sodium metasilicate nonahydrate. The microbial cultures were inoculated from the axenically grown cyanobacterium *Synechococcus* sp. PCC 7002 (referred from herein as *Synechococcus*) grown on agar plates and subsequently incubated in modified liquid A+ marine media at 30°C (Mloszewska et al. 2018). The original A+ medium that was designed for growing marine cyanobacteria species was modified to exclude ethylenediaminetetraacetic acid (EDTA) such that formation of Fe minerals was not chelated during the experiments. The optical density

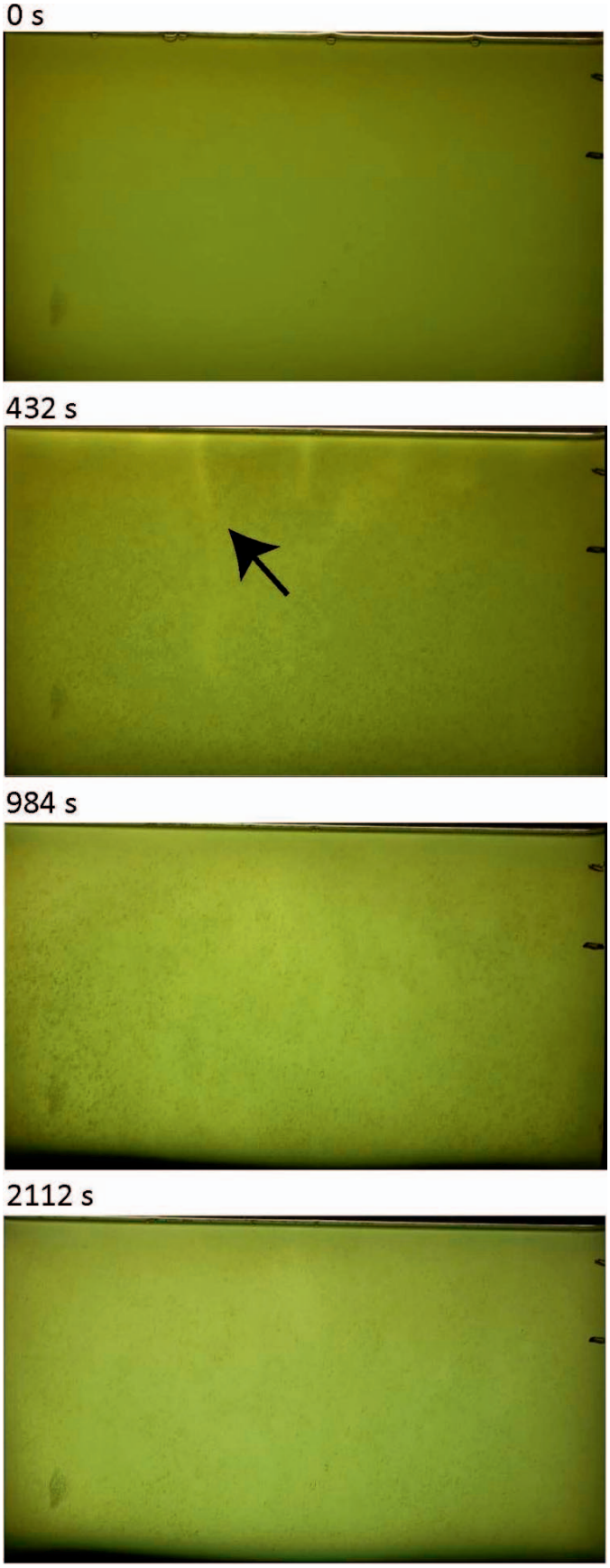

TABLE 1.—*A list of 11 experiments conducted in this paper with initial conditions, settling forms, and average sedimentation velocity.*

Experiment	pH	Fe (II) Concentration (μM)	Settling Form	Average Sedimentation Velocity (cm/s)
1	11	225	Concentration Front	0.0284 (± 0/0001)
2	11	450	Concentration Front	0.0302 (± 0.0017)
3	11	600	Concentration Front	0.0362 (± 0.0020)
4	11	900	Concentration Front	0.0379 (± 0.0030)
5	11	1200	Concentration Front	0.0353 (± 0.0016)
6	11	1500	Concentration Front	0.0414 (± 0.0016)
7	11	1800	Concentration Front	0.0447 (± 0.0012)
8	10	1800	Concentration Front	0.0398 (± 0.0016)
9	9	1800	Plumes	0.0905 (± 0.0128)
10	8	1800	Plumes	0.0738 (± 0.0049)
11	7	1800	Plumes	0.0360 (± 0.0050)

of the *Synechococcus* cultures at 750 nm was closely monitored, and cultures were harvested for experiments when the optical density reached 0.5 or higher.

As a general background to the Precambrian conditions we aim to mimic, concentrations of dissolved Fe(II) in the bulk oceans may have varied between the range of 30 μM (Holland 1973) to 500 μM (Morris 1993), but in the vicinity of hydrothermal plumes it is possible that dissolved Fe(II) concentrations may have been 1–2 orders of magnitude higher than today (Kump and Seyfried 2005); the concentration of Fe(II) effused from some modern deep-sea vents is 1800 μM (Edmond et al. 1982). Recent work also suggests that in the presence of dissolved silica, whose concentration was potentially 2200 μM in Precambrian seawater (Konhauser et al. 2007), the initial water-column precipitate may have been a Fe(III)–Si gel (Zheng et al. 2016).

To demonstrate the settling process of aggregates under various chemical conditions, as well as the relationship between sedimentation velocity with different chemical parameters, eleven experiments were conducted over a range of pH values and initial Fe(II) concentrations (Table 1).

Experimental mixtures of chemicals and biomass were created as follows. Ultrapure water was supplemented with NaCl and $NaHCO_3$ to final concentrations of 0.56 M and 70 μM, respectively. Subsequently, a concentrated liquid cyanobacteria culture (OD 750 nm approximately equals to 0.2) and Si (2200 μM) were added. The pH of this mixture was rapidly adjusted using either concentrated HCl or NaOH to obtain the indicated pH.

The final mixture was immediately added to the culture tank and the recording started. Simultaneously, an initially anaerobic Fe(II) stock solution was added via a sterile syringe to obtain the indicated final concentrations ranging from 225 μM to 1800 μM. Note that experiments were not conducted at the lower concentration range of dissolved iron predicted for in the Archean (30 μM; Holland 1973) because our focus here was to oxidize sufficient Fe(II) so that flocculation of a ferric oxyhydroxide (e.g., ferrihydrite) would occur over the time course of these experiments. The mixture was stirred vigorously with a sterile plastic pasture pipette to ensure a homogeneous state, and then the mixture was left undisturbed with cyanobacteria–iron aggregates

←

FIG. 4.—Images from a plume experiment with pH = 9 and initial Fe(II) concentration of 1800 μM. In each image the field of view is 20 cm wide by 10 cm tall. The plume that was used to determine sedimentation velocity is indicated by the arrow. Note the color difference between the developed plumes and their surroundings, showing the co-deposition of cyanobacteria cells and ferrihydrite.

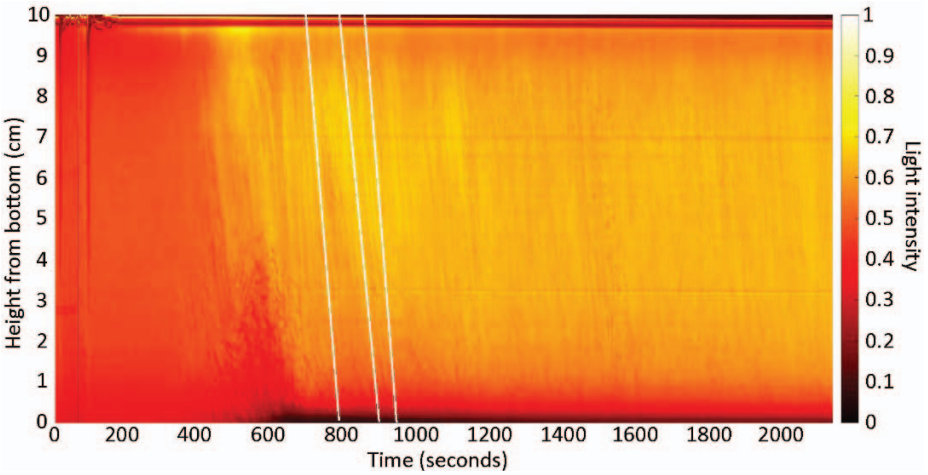

FIG. 5.—Vertical time series of a single vertical slice taken from the experiment shown in Figure 4.

forming and settling in the relatively quiescent fluid until the end of the recording process. All of the experiments were left open to the atmosphere because we were mainly interested in elucidating the physical settling process after formation of the aggregates, not the oxidation of Fe(II).

To confirm the mineralogy of aggregates formed in this study, final sedimented aggregates from selected experiments with pH values from 7 to 11 were treated with 0.2 M ammonium-oxalate solution, of which the pH was adjusted to 3.25 using 0.2 M oxalic acid. This method was chosen because it is commonly used to extract amorphous or poorly crystalline ferric oxyhydroxides such as ferrihydrite (Schwertmann 1964; Stoppe et al. 2015; Stranghoener et al. 2018).

Video Processing

The movies were pre-processed using the open-source software "ffmpeg" to reduce file size. This was done by cropping the image to include only the 10-cm-deep backlit part of the tank and then constructing a time-lapse movie using one frame every second and catenating those frames to form a new movie. This resulted in a video that ran 24 times faster than the original recording.

After pre-processing, the program MATLAB (https://www.mathworks.com) was used to input and digitize the movies and, from this, construct vertical time series images from which the aggregates descent could be measured. Specifically, how the time series were constructed depended on the mechanism by which aggregates settled. Based on our observation of all preliminary experiments, aggregates settled exclusively through one of two mechanisms: 1) a sediment-concentration front developed and descended uniformly across the span of the tank, capturing most of the suspended particles with it, or 2) one or more localized plumes developed with cell–mineral aggregates descending in the plumes but also rising in the ambient fluid surrounding the plumes, as occurs in convective cells.

Calculations for the Settling-Front Mechanism

At pH values above 9, the cell–mineral aggregates grew to form large aggregates that were visible by eye; estimated sizes were measured on Adobe Illustrator from individual frames selected from the video recordings based on the dimension of the water tank. The aggregates then formed a sediment concentration front that descended quickly in the tank, with settling times ranging from 5 to 30 minutes (Fig. 2). In this case, we used MATLAB to construct vertical time series of the horizontally averaged light intensity. Specifically, from each frame of the time-lapse movie, the horizontal average produced a plot of mean light intensity as a function of height from the bottom of the tank. The successive intensity-versus-height plots were then stacked side by side to produce a plot of light intensity as a function of height and time. The descending concentration front was then highlighted by applying a false-color scheme (Fig. 3). To quantify the sedimentation velocity of the front, three contours of constant light intensity were plotted on top of the vertical time series. The contours were chosen from 20% to 75% of the maximum light intensity occurring with no particles in suspension. Shortly after the settling front formed, it was found to descend at nearly constant rate. By applying best-fit lines to the three contours using Adobe Illustrator, estimates of the front sedimentation velocity and its error were determined.

Calculations for the Plume Mechanism

It was uncommon to observe a well-defined descending concentration front when the pH was lower than 9. Instead, the aggregates grew slowly over several hours. Although individual aggregates were difficult to observe by eye, they interacted collectively to descend as horizontally localized and sediment-laden convective cells or plumes, which are horizontally localized buoyancy-driven flows caused by negative buoyancy as a result of aggregate sedimentation (Turner 1973) (Fig. 4). Sedimentation of initially suspended aggregates also caused the density of the interstitial fluid to decrease below the density of the ambient fluid, which further triggered corresponding upward circulation, also known as vortex tips. These vortex tips were observed on either side of the plume (Fohrmann et al. 1998). The validity of our experimental approach to real-life sedimentation was reflected in the plumes observed being similar to those formed via sedimentation of natural sediment in buoyant turbulent suspensions under laboratory settings such as those described in McCool and Parsons (2004). The sedimentation velocity of aggregates in the descending plumes was measured to be the speed of a single descending plume. Thus, the sedimentation velocity accounts only for the maximum descending velocity of a single plume formed in the solution, and not the velocity at which all the aggregates eventually settled. MATLAB was used to extract just a single vertical time slice through each frame located at the horizontal position of the plume where it initially formed. The successive images of light intensity versus height were then stacked to construct a vertical time series, as shown in Figure 5. On each vertical time series, the slopes of three lines that depict descending regions of relatively high light intensity were chosen for quantification of sedimentation velocity and their errors.

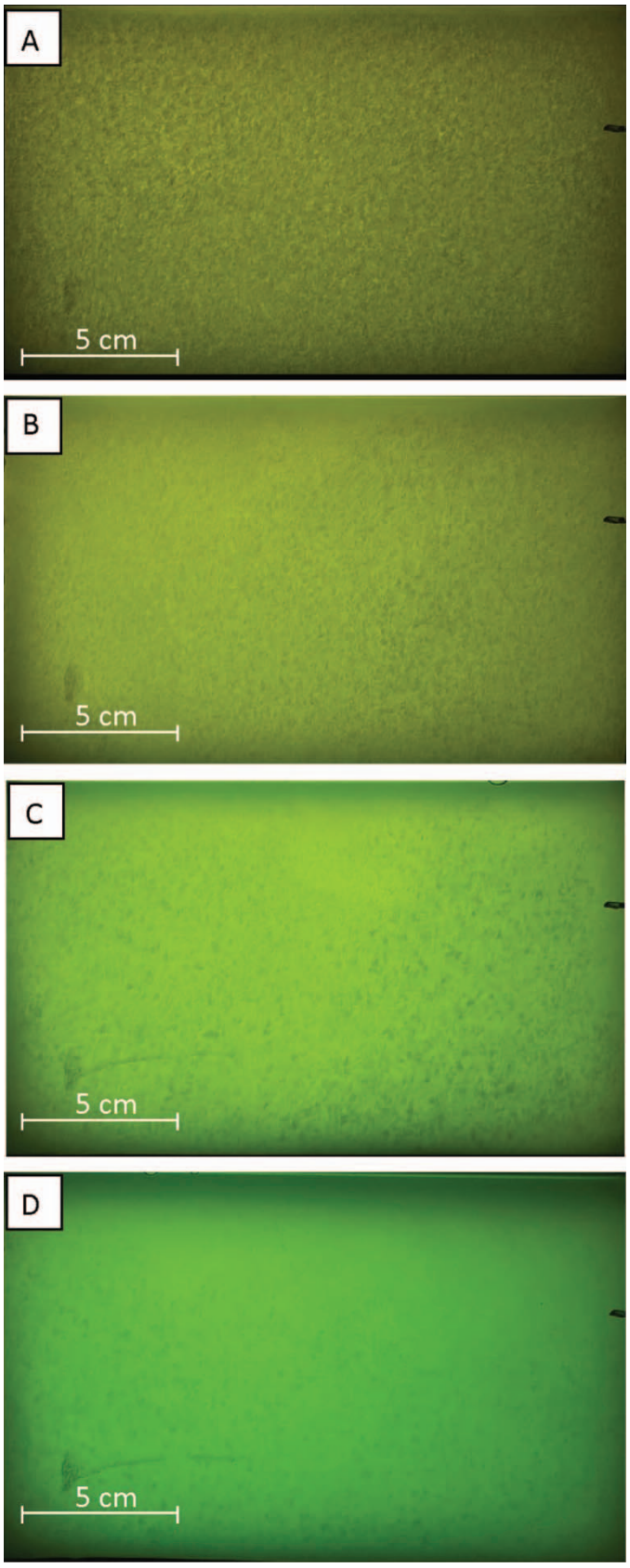

FIG. 6.—Aggregate size comparison from four settling-front experiments at pH = 11. **A)** Fe(II) concentration = 1800 μM; **B)** Fe(II) concentration = 1200 μM; **C)** Fe(II) concentration = 600 μM; and **D)** Fe(II) concentration = 225 μM. Interconnected aggregates are shown in Parts A and B. Individual aggregates are shown in Parts C and D.

RESULTS

From the 11 experiments that were conducted for this study, cell–Fe(III) mineral aggregates settled in the form of a concentration front in eight experiments, seven of which were at pH 11 and 1 was at pH 10. In the remaining three experiments, aggregates settled in the form of plumes at lower pH values from 7 to 9 (Table 1). Upon treatment with ammonium oxalate, sedimented aggregates from selected experiments immediately became soluble, indicating that aggregates formed in our experiments are amorphous ferrihydrite.

The sedimentation velocity measured in settling-front experiments ranged from 0.0284 cm s^{-1} to 0.0447 cm s^{-1} with increasing initial Fe(II) concentration. At higher initial Fe(II) concentrations from 1800 to 1200 μM, aggregates were densely distributed across the water tank. As a result, these aggregates interacted with each other and collected to produce larger aggregates on the order of 2 cm in diameter (Fig. 6A, B). However, at lower Fe(II) concentrations, from 900 to 225 μM, aggregates were more sparsely distributed, and thus some individual aggregates could be identified and measured. Visible aggregates ranged in scale from 0.2 to 0.5 cm (Fig. 6C, D). At pH 11, the seven settling-front experiments with different initial Fe(II) concentration from 225 μM to 1800 μM showed increasing sedimentation velocity with increasing initial Fe(II) concentrations and corresponding larger aggregate sizes (Fig. 7).

The three experiments where aggregates settled in the form of plumes had pH values ranging from 7 to 9, while the initial Fe(II) concentration was fixed at 1800 μM. The calculated sedimentation velocity varied from 0.036 (± 0.005) to 0.090 (± 0.013) cm s^{-1}, increasing steadily with increasing pH (Fig. 8).

DISCUSSION

Applying Stokes' Law (Eq. 1) to calculate the sedimentation velocity of chemical flocculants, such as cyanobacteria–ferrihydrite aggregates, that form in suspension and settle through a water column, provides only a crude approximation. First, naturally occurring aggregates are irregularly shaped, owing to their porous nature (Schädler et al. 2008). Second, aggregate size constantly changes from their initial formation in the water column to deposition, and it is thus challenging to measure accurately the particle size regardless of the size of the sample pool. Third, we observed complex settling mechanisms in which aggregates interacted with each other to settle collectively through the water column either as convective cells or plumes.

We evaluated the relationship between our measured sedimentation velocities with rates estimated by Stokes' law, using Equation 1 with $\mu = 1.02 \times 10^{-2}$ g cm^{-1} s^{-1}, $g = 981$ cm s^{-2}, and ambient fluid density $\rho_f = 1.022$g cm^{-3}. The effective radius of the aggregate was taken to be 0.2 cm when the Fe(II) concentration was 225 μM, and 2 cm when the Fe(II) concentration was 1800 μM (Konhauser et al. 2005). Assuming a particle is conservatively composed of 1% ferric oxide (with a density of 3.8 g cm^{-3}) and 99% ambient fluid in its pores, we estimate the effective particle density ρ_P to be 1.05 g cm^{-3}. These parameters predict a wide range of sedimentation velocities from 30 cm s^{-1} to 3×10^4 cm s^{-1}, which are several orders of magnitude faster than what was measured here. This drastic difference highlights how Stokes' law cannot be applied when calculating the sedimentation velocity of such chemical sediments.

Our results provide four major insights into the chemical and mechanistic mechanisms contributing to BIF formation. First, the settling processes of cyanobacteria–ferrihydrite aggregates are more complicated than previously anticipated from Stokes' law-based calculations. Depending on a combination of pH and initial Fe(II) concentration, the form of aggregates descending through a water column can be classified into three categories: 1) a concentration front that settles at a steady rate, 2) settling as single or multiple plumes, and 3) slow dispersion that takes several hours

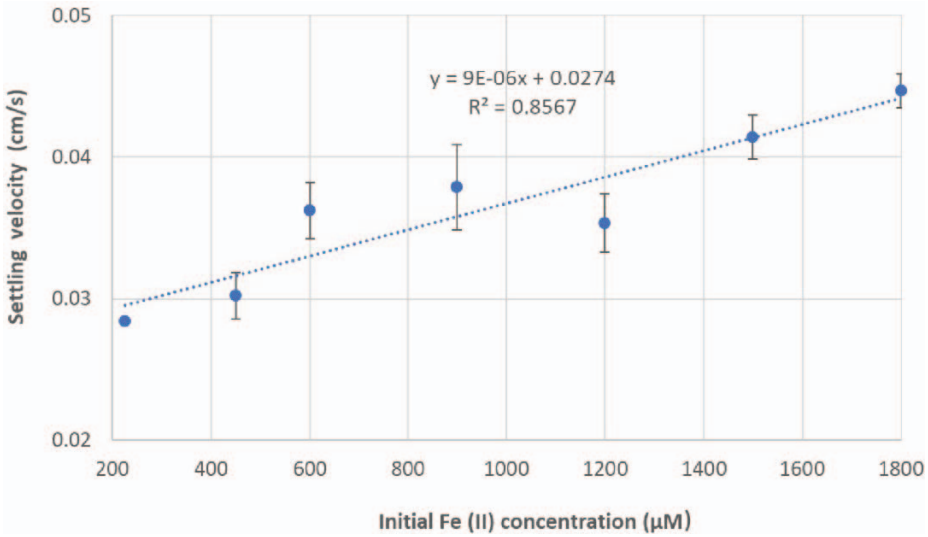

FIG. 7.—Average sedimentation velocity of concentration-front mechanism at pH 11 relative to initial Fe(II) concentration from 225 μM to 1800 μM.

to even days. We focused on the first two mechanisms because the third mechanism was observed only at pH below 7, and the settling velocity was too slow to be measured and modeled in MATLAB. Aggregates settled in the form of a concentration front over a range of initial Fe(II) concentrations at pH 10 or above. Although pH 10 is higher than the maximum pH value of 8.6 that was predicted in the Archean oceans (Krissansen-Totton et al. 2018), higher pH values could have occurred episodically when high-pH and silica-rich hydrothermal fluids were introduced to shallow marine environments (Sekine et al. 2015). Our results indicate that, under these conditions, cyanobacterial–ferrihydrite aggregates could have settled to the continental shelf seafloor in the form of a concentration front. On the other hand, when the pH was below 10 but above 6, our data indicate that aggregates exclusively settled in the form of plumes. In sum, these results imply that plume deposition may have been more predominant in the nearshore Archean water column.

Second, sedimentation velocity of cyanobacteria–ferrihydrite aggregates depended on a combination of pH and initial Fe(II) concentrations (Figs. 7, 8). Qualitatively, our result from concentration-front experiments is consistent with Stokes' Law, Equation 1, which predicts that the terminal velocity of a settling sphere is proportional to the density difference of the particle and fluid and increases as the square of the size of the objects. Although the iron precipitate in our experiments is ferrihydrite, with a known density of 3.8 g cm^{-3}, the actual density of an aggregate must take into account the volume fraction of ambient fluid within the aggregate.

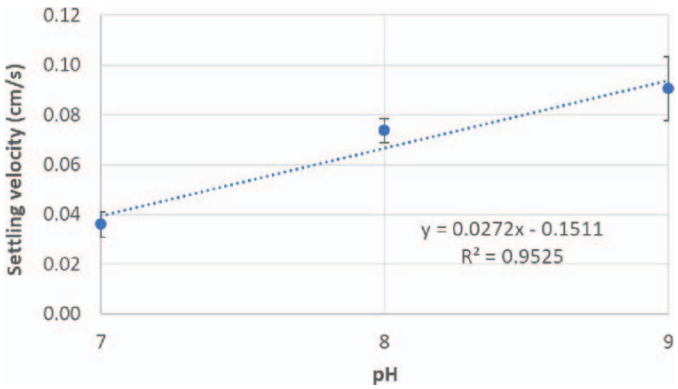

FIG. 8.—Average sedimentation velocity of plume mechanism at initial Fe(II) concentration of 1800 μM relative to pH values from 7 to 9.

Assuming this fraction comprises a fixed ratio as the aggregate expands, our results indicated that the primary factor governing the sedimentation velocity was aggregate size that is directly dependent on initial Fe(II) concentration. Meanwhile, our result from plume experiments showed that sedimentation velocity increased not only with increasing initial Fe(II) concentration but also with increasing pH. The increased sedimentation velocity at higher pH is likely related to the rate of Fe(II) oxidation to Fe(III) and the subsequent hydrolysis of dissolved Fe(III) to form solid-phase ferrihydrite (Singer and Stumm 1970). Moreover, the surface charge of the ferrihydrite surface changes with increasing pH, from predominantly $> FeOH_2^+$ below pH 4 to $>$ Fe(OH) between pH 4 and 12 (Millero 2001). Increased surface exposure of hydroxy groups (OH) facilitates hydrogen bonding between ferric hydroxide particles, thus leading to greater polymerization and flocculation (Dzombak and Morel 1990).

Third, *Synechococcus* cells were observed to co-deposit with ferrihydrite, contributing to the accumulation of sedimented material under every geochemical condition tested (Figs. 2, 4). These findings indicate a tight physical association between *Synechococcus* cells with ferrihydrite *in vivo*, confirming the observations described by Thompson et al. (2019). In contrast, tight associations were not observed between anoxygenic photosynthesis bacteria and Fe(III) minerals (Konhauser et al. 2005; Gauger et al. 2016; Schad et al. 2019). Importantly, if cyanobacteria were the dominant biological mechanism for Fe(II) oxidation (versus photoferrotrophs), then the co-deposition we observed with the cell–mineral aggregates implies that biomass must have been deposited to the ancient seafloor. This biomass, in turn, would subsequently have served as a suitable electron donor to various respiratory processes during diagenesis, such as dissimilatory Fe(III) reduction (Konhauser et al. 2005). This specific biochemical deposition process shown here will contribute to the explanation of the origin of both the common secondary iron minerals in BIF, such as siderite ($FeCO_3$) (Köhler et al. 2013) or magnetite (Li et al. 2013), as well as the low organic-carbon contents preserved in BIF (Gole and Klein 1981).

Fourth, the maximum sedimentation velocity of ferrihydrite–cell aggregates at pH 7 with 1800 μM initial Fe(II) concentration is 0.0360 (± 0.0050) cm/s. This value is approximately 30% lower than the sedimentation velocity predicted by Stokes' Law using similar aggregates (0.05 cm/s) at pH 6.8 (Kappler and Newman 2004; Konhauser et al. 2005). It should be noted that even considering that we observed increases in the sedimentation velocity with Fe(II) concentration, the low predicted Fe(II) concentration in Archean oceans (30–500 μM; Holland 1973; Morris

1993) compared to the 1800 μM used here would suggest that the functional sedimentation velocity of aggregates during BIF deposition would have been substantially lower than reported here.

The observations presented here are crucial because they provide new insights into the conditions and mechanisms contributing to BIF deposition. Previous studies have attempted to calculate annual iron fluxes from the water column to the seafloor during BIF deposition as a means of determining not only the time scale for BIF deposition but also the iron concentration that existed in the paleo-oceans to supply BIF. Our findings suggest that iron fluxes have been significantly overestimated, potentially altering the time scale for BIF deposition compared to estimates calculated from Stokes' Law. In addition, the corresponding Reynolds number of the aggregates size we observed under the concentration-front mechanism ranges between 2 and 4, significantly above the limiting Reynolds number of 0.1, below which Stokes' law is applicable. Thus, in the Archean ocean, utilization of Stokes' Law is not sufficient to accurately describe BIF deposition. Combined, our observations provide informative mechanistic data for incorporation into future modeling of BIF deposition, specifically that the formation and deposition of ferrihydrite–cyanobacteria aggregates occur via uniquely independent mechanisms inherently dependent on pH and initial Fe concentration.

CONCLUSIONS

To understand the rate of BIF accumulation, it is crucial to understand the range of sedimentation velocity for ferrihydrite–cell aggregates, which are considered as one of the primary sediments contributing to BIFs. In this work, we use a new method that allows real-time observation of the settling processes associated with the formation of (bio)chemical sediments. Using a range of pH and Fe(II) concentrations, we determined the sedimentation velocity of ferrihydrite–cyanobacteria aggregates under a range of chemical conditions. Importantly, our measured sedimentation velocities are significantly lower than previously proposed, based on Stokes' Law. This observation is a significant consideration to incorporate into models that predict the rate of BIF accumulation. Our results substantially refine previous estimates based on Stokes' law, and crucially indicate that both pH and initial Fe(II) concentration combine to determine the mechanism and sedimentation velocity of BIF precursor sediments.

ACKNOWLEDGMENTS

This work was supported by Natural Sciences and Engineering Research Council of Canada Discovery Grants to KOK (RGPIN-165831), BRS (RGPIN-2015-04758), MKG (RGPIN-2020-05138), and GWO (RGPIN-171319). Yuhao Li gratefully acknowledges Tiffany Playter for some of the initial ideas pertaining to this study, Denise Whitford and Logan Brand for their assistance with cell cultures, and Kaarel Mand and Weiduo Hao for their valuable insights and discussions.

REFERENCES

Arnold, H.D., 1911, LXXIV. Limitations imposed by slip and inertia terms upon Stokes' law for the motion of spheres through liquids: The London, Edinburgh, and Dublin Philosophical Magazine and Journal of Science, v. 22, p. 755–775.

Bekker, A., Slack, J.F., Planavsky, N., Krapez, B., Hofmann, A., Konhauser, K.O., and Rouxel, O.J., 2010, Iron formation: the sedimentary product of a complex interplay among mantle, tectonic, oceanic, and biospheric processes: Economic Geology, v. 105, p. 467–508.

Beukes, N.J., and Gutzmer, J., 2008, Origin and paleoenvironmental significance of major iron formations at the Archean–Paleoproterozoic boundary: Reviews in Economic Geology, v. 15, p. 5–47.

Dzombak, D.A., and Morel, F.M.M., 1990, Surface Complexation Modeling: Hydrous Ferric Oxide: John Wiley & Sons, p. 89–90.

Edmond, J.M., Von Damm, K.L., McDuff, R.E., and Measures, C.I., 1982, Chemistry of hot springs on the East Pacific rise and their effluent dispersal: Nature, v. 297, p. 187–191.

Fohrmann, H., Backhaus, J.O., Blaume, F., and Rumohr, J., 1998, Sediments in bottom-arrested gravity plumes: numerical case studies: Journal of Physical Oceanography, v. 28, p. 2250–2274.

Gauger, T., Byrne, J.M., Konhauser, K.O., Obst, M., Crowe, S., and Kappler, A., 2016, Influence of organics and silica on Fe(II) oxidation rates and cell–mineral aggregate formation by the green-sulfur Fe(II)-oxidizing bacterium *Chlorobium ferrooxidans* KoFox: implications for Fe(II) oxidation in ancient oceans: Earth and Planetary Science Letters, v. 443, p. 81–89.

Gole, M.J., and Klein, C., 1981, Banded iron formations through much of Precambrian time: Journal of Geology, v. 89, p. 169–183.

Guazzelli, É., and Hinch, J., 2011, Fluctuations and instability in sedimentation: Annual Review of Fluid Mechanics, v. 43, p. 97–116.

Holland, H.D., 1973, The oceans: a possible source of iron in iron formations: Economic Geology, v. 68, p. 1169–1172.

Kappler, A., and Newman, D.K., 2004, Formation of Fe(III)-minerals by Fe(II)-oxidizing photoautotrophic bacteria: Geochimica et Cosmochimica Acta, v. 68, p. 1217–1226.

Kendall, B., Reinhard, C.T., Lyons, T.W., Kaufman, A.J., Poulton, S.W., and Anbar, A.D., 2010, Pervasive oxygenation along late Archaean ocean margins: Nature Geoscience, v. 3, p. 647–652.

Klein, C., 2005, Some Precambrian banded-iron formations (BIFs) from around the world: their age, geologic setting, mineralogy, metamorphism, geochemistry, and origin: American Mineralogist, v. 90, p. 1473–1499.

Köhler, I., Konhauser, K.O., Papineau, D., Bekker, A., and Kappler, A., 2013, Biological carbon precursor to diagenetic siderite with spherical structures in iron formations: Nature Communications, v. 4, article 1741.

Konhauser, K.O., Newman, D.K., and Kappler, A., 2005, The potential significance of microbial Fe(III) reduction during deposition of Precambrian banded iron formations: Geobiology, v. 3, p. 167–177.

Konhauser, K.O., Amskold, L., Lalonde, S.V., Posth, N.R., Kappler, A., and Anbar, A., 2007, Decoupling photochemical Fe(II) oxidation from shallow-water BIF deposition: Earth and Planetary Science Letters, v. 258, p. 87–100.

Konhauser, K.O., Planavsky, N.J., Hardisty, D.S., Robbins, L.J., Warchola, T.J., Haugaard, R., Lalone, S.V., Partin, C.A., Onnk, P.B.H., Tsikos, H., Lyons, T.W., Bekker, A., and Johnson, C.M., 2017, Iron formations: a global record of Neoarchaean to Palaeoproterozoic environmental history: Earth-Science Reviews, v. 172, p. 140–177.

Konhauser, K.O., Robbins, L.J., Alessi, D.S., Flynn, S.L., Gingras, M.K., Martinez, R.E., Kappler, A., Swanner, E.D., Li, Y.-L., Crowe, S.A., Planavsky, N.J., Reinhard, C.T., and Lalonde, S.V., 2018, Phytoplankton contributions to the trace-element composition of Precambrian banded iron formations: The Geological Society of America, Bulletin, v. 130, p. 941–951.

Krissansen-Totton, J., Arney, G.N., and Catling, D.C., 2018, Constraining the climate and ocean pH of the early earth with a geological carbon cycle model: National Academy of Sciences, Proceedings, v. 115, p. 4105–4110.

Kump, L.R., and Seyfried, W.E., 2005, Hydrothermal Fe fluxes during the Precambrian: effect of low oceanic sulfate concentrations and low hydrostatic pressure on the composition of black smokers: Earth and Planetary Science Letters, v. 235, p. 654–662.

Li, Y.-L., Konhauser, K.O., Kappler, A., and Hao, X.-L., 2013, Experimental low-grade alteration of biogenic magnetite indicates microbial involvement in generation of banded iron formations: Earth and Planetary Science Letters, v. 361, p. 229–237.

McCool, W.W., and Parsons, J.D., 2004, Sedimentation from buoyant fine-grained suspensions: Continental Shelf Research, v. 24, p. 1129–1142.

Millero., F., 2001, Speciation of metals in natural waters: Geochemical Transactions, v. 2, p. 57–65.

Mloszewska, A.M., Cole, D.B., Planavsky, N.J., Kappler, A., Whitford, D.S., Owttrim, G.W., and Konhauser, K.O., 2018, UV radiation limited the expansion of cyanobacteria in early marine photic environments: Nature Communication, v. 9, article number 3088.

Morris, R.C., 1993, Genetic modelling for banded-iron formation of the Hamersley Group, Pilbara craton, western Australia: Precambrian Research, v. 60, p. 243–286.

Phoenix, V.R., Adams, D.G., and Konhauser, K.O., 2000, Cyanobacterial viability during hydrothermal biomineralization: Chemical Geology, v. 169, p. 329–338.

Playter, T., Konhauser, K.O., Owttrim, G.W., Hodgson, C., Warchola, T., Mloszewska, A.M., Sutherland, B.R., Bekker, A., Zonneveld, J.-P., Pemberton, S.G., and Gingras, M., 2017, Microbe–clay interactions as a mechanism for the preservation of organic matter and trace metal biosignatures in black shales: Chemical Geology, v. 459, p. 75–90.

Posth, N.R., Huelin, S., Konhauser, K.O., and Kappler, A., 2010, Size, density and composition of cell–mineral aggregates formed during anoxygenic phototrophic Fe(II) oxidation: impact on modern and ancient environments: Geochimica et Cosmochimica Acta, v. 74, p. 3476–3493.

Posth, N.R., Konhauser, K.O., and Kappler, A., 2013, Microbiological processes in banded iron formation deposition: Sedimentology, v. 60, p. 1733–1754.

Posth, N.R., Canfield, D.E., and Kappler, A., 2015, Biogenic Fe (III) minerals: from formation to diagenesis and preservation in the rock record: Earth-Science Reviews, v. 135, p. 103–121.

Rasmussen, B., Muhling, J.R., Suvorova, A., and Krapež, B., 2017, Greenalite precipitation linked to the deposition of banded iron formations downslope from a late Archean carbonate platform: Precambrian Research, v. 290, p. 49–62.

Robbins, L.J., Funk, S.P., Flynn, S.L., Warchola, T.J., Li, Z., Lalonde, S.V., Rostron, B.J., Smith, A.J., Beukes, N.J., de Kock, M.O., and Heaman, L.M., 2019, Hydrogeological

constraints on the formation of Palaeoproterozoic banded iron formations: Nature Geoscience, v. 12, p. 558–563.

Schad, M., Halama, M., Bishop, B., Konhauser, K.O., and Kappler, A., 2019, Temperature fluctuations in the Archean ocean as trigger for varve-like deposition of iron and silica minerals in banded iron formation: Geochimica et Cosmochimica Acta, v. 265, p. 386–412.

Schädler, S., Burkhardt, C., and Kappler, A., 2008, Evaluation of electron microscopic sample preparation methods and imaging techniques for characterization of cell–mineral aggregates: Geomicrobiology Journal, v. 25, p. 228–239.

Schwertmann, U., 1964, Differenzierung der Eisenoxide des Bodens durch Extraktion mit Ammoniumoxalat-Lösung: Zeitschrift für Pflanzenernährung, Düngung, Bodenkunde, v. 105, p. 194–202.

Sekine, Y., Shibuya, T., Postberg, F., Hsu, H., Suzuki, K., Masaki, Y., Kuwatani, T., Mori, M., Hong, P.K., Yoshizaki, M., Tachibana, and Sirono, S., 2015, High-temperature water–rock interactions and hydrothermal environments in the chondrite-like core of Enceladus: Nature Communications, v. 6, article 8604.

Singer, P.C., and Stumm, W., 1970, Acid mine drainage: the rate-determining step: Science, v. 167, p. 1121–1123

Smith, A.J.B., 2015, The life and times of banded iron formations: Geology, v. 43, p. 1111–1112.

Smith, A.J.B., Beukes, N.J., and Gutzmer, J., 2013, The composition and depositional environments of Mesoarchean iron formations of the West Rand Group of the Witwatersrand Supergroup, South Africa: Economic Geology, v. 108, p. 111–134.

Smith, A.J.B., Beukes, N.J., Gutzmer, J., Czaja, A.D., Johnson, C.M., and Nhleko, N., 2017, Oncoidal granular iron formation in the Mesoarchaean Pongola Supergroup, southern Africa: textural and geochemical evidence for biological activity during iron deposition: Geobiology, v. 15, p. 731–749.

Stokes, G.G., 1850, On the effect of the internal friction of fluids on the motion of pendulums: Cambridge Philosophical Society, Transactions, v. 9, p. 8–109.

Stoppe, N., Amelung, W., and Horn, R., 2015, Chemical extraction of sedimentary iron oxy (hydr) oxides using ammonium oxalate and sodium dithionite revisited: an explanation of processes in coastal sediments: Agro Sur, v. 43, p. 11–17.

Stranghoener, M., Schippers, A., Dultz, S., and Behrens, H., 2018, Experimental microbial alteration and Fe mobilization from basaltic rocks of the ICDP HSDP2 drill core, Hilo, Hawaii: Frontiers in Microbiology, v. 9, p. 1252.

Sutherland, B.R., Barrett, K.J., and Gingras, M.K., 2015, Clay settling in fresh and salt water: Environmental Fluid Mechanics, v. 15, p. 147–160.

Thompson, K.J., Kenward, P.A., Bauer, K.W., Warchola, T., Gauger, T., Martinez, R., Simister, R.L., Michiels, C.C., Lirós, M., Reinhard, C.T., Kappler, A., Konhauser, K.O., and Crowe, S.A., 2019, Photoferrotrophy, deposition of banded iron formations, and methane production in Archean oceans: Science Advances, v. 5, article 11.

Turner, J.S., 1973, Buoyant Convection from Isolated Sources, *in* Batchelor, G.K., and Miles, J.W., eds., Buoyancy Effects in Fluid: Cambridge University Press, p. 165–206.

Wray, E.M., 1977, Stokes' law revisited: Physics Education, v. 12, p. 300–303.

Zheng, X.-Y., Beard, B.L., Reddy, T.R., Roden, E.E., and Johnson, C.M., 2016, Abiologic silicon isotope fractionation between aqueous Si and Fe(III)–Si gel in simulated Archean seawater: implications for Si isotope records in Precambrian sedimentary rocks: Geochimica et Cosmochimica Acta, v. 187, p. 102–122.

Received 8 July 2020; accepted 1 February 2021.